

High Sodium-Ion Battery Capacity in Sulfur-Deficient Tin(II) Sulfide Thin Films with a Microrod Morphology

Zening Zhu, Geoffrey Hyett, Gillian Reid, Fred Robinson, Giannantonio Cibin, and Andrew L. Hector*

Sulfur-deficient SnS thin films for sodium-ion battery anode application are prepared using aerosol-assisted chemical vapor deposition. Growth directly onto the metal foil current collector forms sulfur-deficient SnS microrod structures via a vapor–liquid–solid growth mechanism, with 92 nm average SnS crystallite size and an 800 nm film thickness. The sulfur deficiency is demonstrated with energy-dispersive X-ray analysis, powder X-ray diffraction, and X-ray absorption near-edge structure analyses. This sulfur-deficient SnS material demonstrates a very high capacity in sodium half cells. The first reduction scan at a specific current of 150 mA g⁻¹ shows a capacity of 1084 mAh g⁻¹. At the 50th cycle the specific capacity is 638 mAh g⁻¹ for reduction and 593 mAh g⁻¹ for oxidation. This capacity is demonstrated for tin sulfide itself without the need for a nanostructured carbon support, unlike previous high capacity SnS anodes in the literature. Both the capacity and ex situ characterization experiments indicate a conversion reaction producing tin, followed by alloying with sodium during reduction, and that both of these processes are reversible during oxidation.

electrochemical inactivity.^[4] Carbon materials are the most widely used SIB anodes, but the reversible capacity is rather low, at ≈350 mAh g⁻¹ at best.^[5] Alloy materials based on Pb, Sb, and Sn are promising high capacity options^[6] but barriers to their wider use include cost, toxicity, and often poor cyclability. Tin has a theoretical capacity of 847 mAh g⁻¹ when fully sodiated to Na₁₅Sn₄, but with a 420% volume change during the alloying/dealloying reactions that results in degradation.^[4,7]

Tin(II) sulfide is a layered semiconductor material with a wide range of electronic applications.^[8] SnS crystallizes with a GeS-type orthorhombic structure, with layers connected by weak Van der Waal's forces along the *c*-axis. The large interlayer spacing provides for easy initial insertion of Na⁺ ions, and SnS has been used several times for LIB and SIB anodes.^[9] SnS has a high theoretical capacity of 1202 mAh g⁻¹ (Equation (1) and (2)).^[4,10]

1. Introduction

Sodium-ion batteries (SIBs) are attractive replacements for lithium-ion batteries (LIBs) due to the much larger earth abundance and lower cost of sodium when compared to lithium.^[1] SIBs share the same working principles as LIBs,^[2] but the sodium ionic radius is 1.55 times larger than that of lithium^[2a] which causes significantly slower ion transport and suitable electrode materials are more difficult to find for SIBs.^[3] Some LIB anode materials, such as graphite, suffer from low capacity and irreversible cyclability with sodium, or even complete

Conversion reaction (capacity 355mAh g⁻¹):

$$\text{SnS} + 2 \text{Na}^+ + 2 \text{e}^- \rightleftharpoons \text{Na}_2\text{S} + \text{Sn} \quad (1)$$


Alloying reaction (capacity 847mAh g⁻¹):

$$4 \text{Sn} + 15 \text{Na}^+ + 15 \text{e}^- \rightleftharpoons \text{Na}_{15}\text{Sn}_4 \quad (2)$$

SnS materials used previously in SIBs are summarized in **Table 1**. There are also various studies in which SnS is combined with different carbon support materials to make composites.^[11] These mitigate the shortcomings of such materials, of large volume changes during intercalation, and the material having low electronic conductivity. Studies into the mechanism of charge storage in SnS in SIB anodes are valuable due to the possibilities of intercalation into the layered structure, conversion, and alloying reactions. Several researchers have used ex situ X-ray diffraction (XRD) methods, but the results vary from case to case. Ultrasmall SnS quantum dots produce a material that is rich in elemental tin after desodiation,^[11c] indicating an irreversible conversion, with similar results observed for SnS@graphene materials.^[4] In both cases, the evidence for this comes from the intensity of the XRD peaks for elemental tin gradually increasing during desodiation.^[4] In contrast, Yu et al. demonstrate loss of Sn metal during desodiation when combining ex situ XRD with X-ray absorption near-edge structure (XANES) measurements.^[12]

Z. Zhu, G. Hyett, G. Reid, F. Robinson, A. L. Hector
School of Chemistry
University of Southampton
Southampton SO17 1BJ, UK
E-mail: A.L.Hector@soton.ac.uk

G. Cibin
Diamond Light Source
Harwell Science and Innovation Campus
Fermi Ave, Didcot OX11 0DE, UK

 The ORCID identification number(s) for the author(s) of this article can be found under <https://doi.org/10.1002/ssstr.202200396>.

© 2023 The Authors. Small Structures published by Wiley-VCH GmbH. This is an open access article under the terms of the Creative Commons Attribution License, which permits use, distribution and reproduction in any medium, provided the original work is properly cited.

DOI: 10.1002/ssstr.202200396

Table 1. Performance of SnS in sodium-ion anode applications.

Material	Initial discharge capacity [mAh g ⁻¹]	Final discharge capacity [mAh g ⁻¹]	Current density [mA g ⁻¹]	Number of cycles	Ref.
Mechanochemically synthesized SnS	≈600	305	125	60	[28]
SnS nanorods	≈520	≈400	125	30	[23]
SnS 3D flowers	≈450	≈300	150	50	[24]
SnS hollow nanofibers	612.9	645.9	100	100	[29]
Sulfur-deficient SnS microrods (high current)	646	368	600	100	Present study
Sulfur-deficient SnS microrods (low current)	849	638	150	50	Present study

In these reports, the increase or decrease in the tin content provides secondary evidence for reversibility.

Coatings of tin chalcogenide thin films have been deposited using different chemical vapor deposition (CVD) techniques, including atmospheric pressure (AP)CVD and low pressure (LP)CVD.^[13] Robinson et al. used LPCVD to deposit SnS onto fused silica substrates using the single source precursors, [¹¹⁹Bu₃Sn(SⁿBu)] and [¹¹⁹Bu₂Sn(SⁿBu)₂].^[14] Single source precursors are widely used in CVD due to the good control of the material composition and the high efficiency of deposition of thin film materials. Aerosol-assisted (AA)CVD works with a wide range of substrates and precursor types.^[15] It has low cost and less stringent precursor volatility requirements than LPCVD.^[16]

Herein, we report sulfur-deficient SnS films with a microrod morphology prepared by AACVD directly onto the metal foil current collector. This anode material offered higher SIB capacities than previously reported for SnS anodes, with stable cycling. By comparing two different tin sulfide anode materials for SIBs, sulfur-deficient SnS microrods had far superior performance compared with stoichiometric SnS films. The large capacity of the sulfur-deficient microrods is attributed to higher conductivity of the material itself, good electronic connectivity with the current collector, and short ion diffusion paths in a structure that can accommodate significant volume change. The mechanism of sodium storage on this sulfur-deficient SnS was investigated by ex situ XRD and XANES, and the conversation/alloying reaction and SnS oxidation state changes during reduction and oxidation have been observed.

2. Experimental Section

2.1. Thin Film Growth by AACVD

SnS thin films were prepared by AACVD, using [¹¹⁹Bu₃Sn(SⁿBu)] (for sulfur-deficient SnS) or [¹¹⁹Bu₂Sn(SⁿBu)₂] (for stoichiometric SnS) as the single-source precursors.^[14] All glassware was washed with deionized water, followed by acetone, and then left in an oven overnight to dry at 80 °C. The anhydrous toluene used in this synthesis was refluxed over molten sodium until dried, before being distilled under N₂. Depositions of sulfur-deficient SnS thin film typically used 0.5 mL precursor (≈1.75 × 10⁻³ mol) in 15 mL dry toluene. Stoichiometric SnS thin films were prepared from 0.3 mL precursor (≈1.05 × 10⁻³ mol) in 5 mL dry toluene. The precursor solution was loaded into a dry precursor bottle inside a dry N₂-purged glove box and then connected to

the AACVD reactor (**Figure 1**) with taps **b** and **c** closed. Coatings were deposited onto 316L stainless steel foil (0.01 × 20 × 100 mm; purchased from Pi-Kem Ltd.). The foil was cleaned with a fine abrasive paper, then placed on the carbon block in the quartz reactor tube, and heated at the required temperature (440–460 °C) with nitrogen gas flowing through tap **a**. When the temperature stabilized, taps **b** and **c** were opened and **a** was closed. A precursor mist was produced using an ultrasonic piezoelectric transducer and then transported via the nitrogen carrier gas (0.1 L min⁻¹) to the CVD reactor tube. The deposition was continued until all of the solution had been transported from the flask.

The tube was allowed to cool to room temperature and removed from the furnace, where the substrates were removed and stored for characterization. The AACVD experiments produced uniform and continuous gray films of SnS with coverages of around 10 cm².

2.2. Thin Film Characterization

Scanning electron microscopy (SEM) used an FEI XL30 with a ThermoFisher UltraDry energy-dispersive X-ray (EDX) detector and a Zeiss Sigma 500 VP with an Oxford Instruments Ultim 170 EDX. Samples were mounted on aluminum stubs with carbon adhesive pads, and samples for cross-sectional measurements were cut with scissors. The SEM images were captured at magnifications of 5000 or 55 000 times with 10 kV accelerating voltage.

Grazing incidence (GI)XRD patterns were collected using a Rigaku SmartLab system (Cu Kα, λ = 1.5418 Å) with a parallel X-ray beam and a Hypix detector in 1D mode. A scan range of 2θ = 10°–80° and a 1° incidence angle was used. Lattice parameters were obtained by fitting the pattern using the Rigaku PDXL software package. Powder XRD data were collected with a 2θ = 20°–80° scan range in Bragg–Brentano geometry on a Bruker D2 Phaser using Cu Kα radiation (λ = 1.5418 Å). The sample used for this was a powder produced by carefully scraping several thin films off their foil substrates. Crystalline phases were compared with the Inorganic Crystal Structure Database (ICSD),^[17] and Rietveld fits used GSAS-2.^[18]

2.3. Sodium Half-Cell Construction and Electrochemical Measurements

The SnS thin film electrodes made by AACVD were punched into 11 mm disks and dried at 70 °C overnight under vacuum,

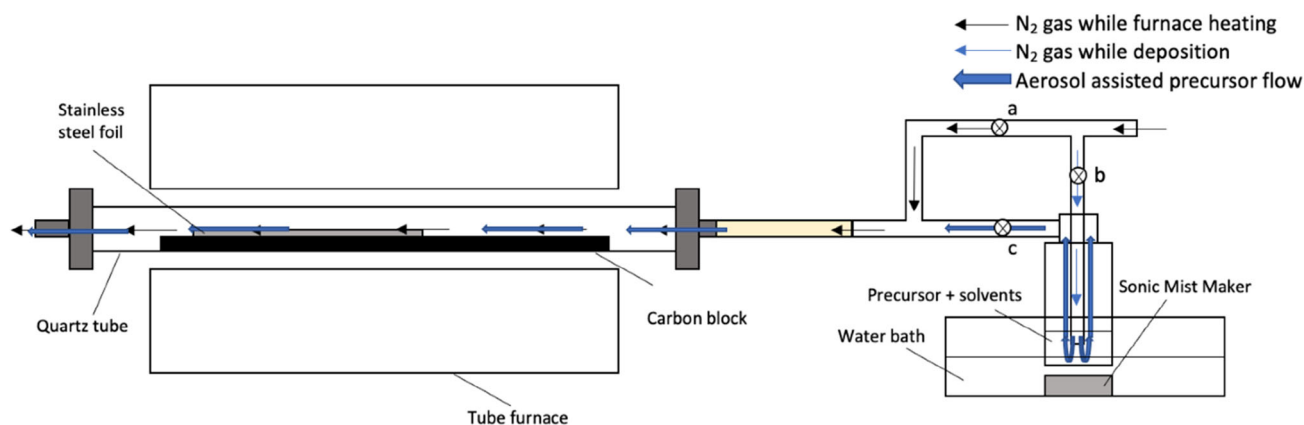


Figure 1. Schematic of the AACVD reactor used to deposit both types of SnS film.

with a mass loading of 0.1–0.4 mg SnS on the stainless steel current collector. Sodium half-cells were assembled in $\frac{1}{2}$ " Swagelok cells in an argon-filled glove box (H_2O , $\text{O}_2 < 1$ ppm). The sodium foil counter electrode for sodium half-cells was made with a slice cut from bulk sodium metal (Aldrich, 99% purity) rolled flat with a round bar and cut to a 11 mm disc. The separator was a glass microfiber filter (Whatman) cut to 12 mm discs and dried at 70 °C under vacuum. The electrolyte was 150 μL of 1 mol dm^{-3} NaPF_6 in 1:1 ethylene carbonate (EC):diethyl carbonate (DEC) with 2 wt% fluoroethylene carbonate (FEC), which was supplied by Fluorochem Ltd.

A Biologic BCS-805 battery cycler and BC-lab software was used to carry out the electrochemical characterization of cells. Galvanostatic charge–discharge cycles used a voltage range of 0.005 to 2 V at 150 mA g^{-1} , with an ambient temperature (25 °C) controlled by an environmental chamber. Data points were recorded every 1 mV, and the cells were cycled 50 times.

2.4. Ex Situ XRD and XANES Measurements

Ex situ measurements were used to measure sulfur-deficient tin sulfide electrodes in sodium half-cells at specific potentials during cell galvanostatic cycling. The Swagelok cells were charged and discharged as usual at 150 mA g^{-1} and when they had reached the target potential were opened in an argon-filled glove box (H_2O , $\text{O}_2 < 1$ ppm). Samples were washed with dry DEC electrolyte solvent, the solvent was allowed to evaporate and samples were loaded into a sealed sample holder designed for use with air-sensitive samples (XRD) or polyfoil bag (XANES). GIXRD used conditions as described above. XANES data were collected across the Sn K-edge (29–30 keV) at the B18 beamline of Diamond Light Source. XANES data were also collected for a tin(II) sulfide standard, which was purchased from Thermo Fisher. Other tin standards (Sn, Na_4Sn , SnO_2) were reused from a previous study.^[7] Comparability between new and previous standards was verified using the spectrum of a tin standard foil that had been placed after the sample detector during data collections.

3. Results and Discussion

3.1. SnS Anode Preparation via AACVD

SnS thin films have previously been deposited on fused silica substrates using LPCVD with the precursors $[\text{Bu}_3\text{Sn}(\text{S}^n\text{Bu})]$ and $[\text{Bu}_2\text{Sn}(\text{S}^n\text{Bu})_2]$.^[14] Initially, AACVD experiments used aluminum foil substrates onto which the SnS thin films were deposited. However, cells made with the aluminum current collectors had poor capacities of around 180 mAh g^{-1} (Figure S1, Supporting Information) due to poor adhesion between the SnS thin films and aluminum foil resulting in poor electronic contact to the active material. Other researchers have found that SnSe produced by CVD on stainless steel foil performed well in LIBs.^[19] Switching from aluminum to stainless steel current collectors (0.01 mm \times 20 mm \times 100 mm) produced much better results. SnS thin films grown by AACVD on stainless steel were stable and had good coverage.

Sulfur-deficient SnS thin films were obtained using the precursor $[\text{Bu}_3\text{Sn}(\text{S}^n\text{Bu})]$. The best deposition temperature with our apparatus was found to be 440 °C (furnace temperature), at a nitrogen flow rate of 0.1 L min^{-1} . A lower temperature of 410 °C did not produce films on the foil and the films became powdery under higher growth temperatures of 460 °C, indicating gas phase particle growth. The powdery films were not suitable for fabrication into electrodes. It took 30 min to heat the AACVD reactor and stabilize the temperature, and the depositions then took approximately 3 h until all the precursor solution had transferred to the reactor. The thin films were uniform and continuous (≈ 800 nm thickness).

Stoichiometric tin sulfide thin films were produced using the precursor $[\text{Sn}^n\text{Bu}_2(\text{S}^n\text{Bu})_2]$. These depositions used 0.3 mL of precursor and 5 mL toluene, at 405 °C, with a nitrogen flow rate of 0.1 L min^{-1} . The coating time was only 30 min, due to the lower solvent and precursor volumes used in this process. The volume of the precursor solution was reduced to avoid a long deposition time because these stoichiometric SnS films were very air sensitive and tin oxide was found after long depositions.

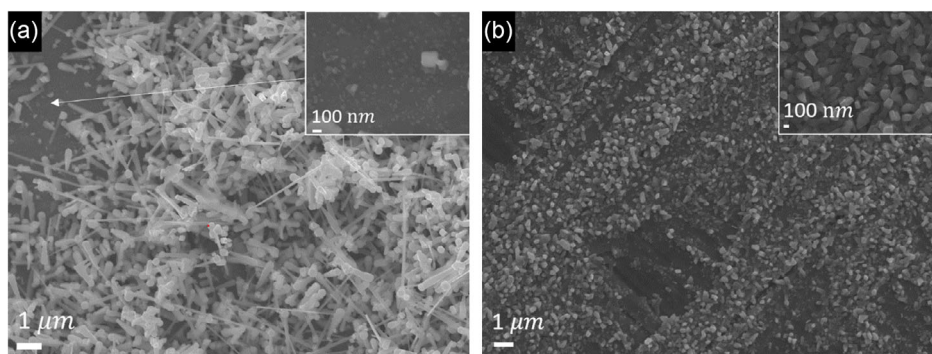


Figure 2. Top-down SEM images for a) sulfur-deficient SnS and b) stoichiometric SnS thin films obtained by AACVD, with 5000 times magnification. The inset in (a,b) is collected at 55 000 times at a substrate surface region.

3.2. Thin Film Characterization

The two precursors produced tin sulfide films that showed completely different crystal morphologies. The sulfur-deficient SnS thin film from $[\text{Bu}_3\text{Sn}(\text{S}^n\text{Bu})]$ contains rods (lengths of $\approx 1 \mu\text{m}$), often with a round head (diameters of $\approx 400 \text{ nm}$) at the end furthest from the substrate (**Figure 2a**). The SEM images of stoichiometric SnS film deposited from $[\text{Sn}^n\text{Bu}_2(\text{S}^n\text{Bu})_2]$ (**Figure 2b**) show block-shaped crystallites with good substrate coverage and a continuous thin film. Both the sulfur-deficient and the stoichiometric SnS films had a continuous layer of small ($\approx 100 \text{ nm}$) crystallites in between the larger deposits, as shown in **Figure 2a** upper right corner, showing that nucleation continues throughout the deposition process.

The elemental composition of both types of tin sulfide films was probed with EDX analysis. The EDX spectra provided the sulfur-deficient and stoichiometric SnS compositions mentioned above (**Figure S2a,b**, Supporting Information). The EDX results showed that the deposition of stoichiometric SnS always resulted in some tin oxide. This issue was avoided by reducing the deposition time to 30 min, and using a small precursor load (0.3 mL precursor and 5 mL solvent). EDX analysis showed that the stoichiometric SnS contained 49 atom% sulfur. The morphology of the sulfur-deficient thin film material was not

well optimized for EDX analysis and variable compositions of 35–40 atom% sulfur were obtained, so the material was scraped off the surface and pressed into a disk. The EDX result was then reproducible with 38 atom% sulfur and 62 atom% tin. All the data analyzed by EDX are presented in Table S2, Supporting Information.

GIXRD was used to determine the pattern of the sulfur-deficient SnS film (**Figure S3**, Supporting Information). However, the iron fluorescence from the substrate (stainless steel foil) reduces the signal:noise ratio and makes the results difficult to use for more detailed analysis. To reduce the impact of the substrate on the XRD results, the film was carefully scraped off the substrate with a scalpel. This was then ground in acetone and transferred dropwise onto an XRD sample holder. Through this, it became clear that some broader peaks in the sulfur-deficient SnS pattern observed by GIXRD were in fact due to the presence of elemental Sn in the SnS film (**Figure 3a**). The sulfur-deficient SnS had an orthorhombic cell with lattice constants of $a = 4.31718(7) \text{ \AA}$, $b = 11.19848(1) \text{ \AA}$, and $c = 3.98854(6) \text{ \AA}$, in good agreement with the range of values found in ICSD for GeS-type SnS ($a = 4.210(7) - 4.336(3) \text{ \AA}$, $b = 11.143(9) - 11.40(2) \text{ \AA}$, and $c = 3.971(3) - 4.091(7) \text{ \AA}$).^[20] Powder XRD also shows tetragonal phase elemental tin with refined lattice constants of $a = 5.83(1) \text{ \AA}$ and $c = 3.1821(3) \text{ \AA}$,

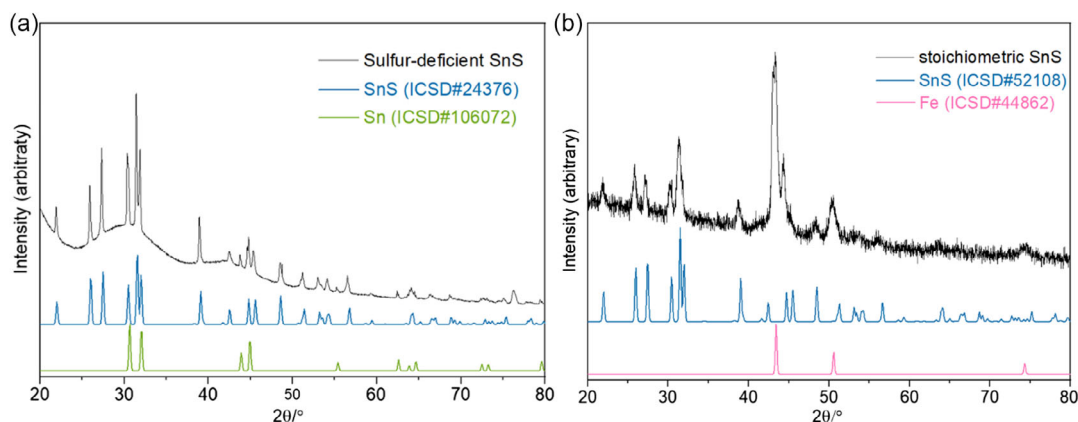


Figure 3. a) Powder XRD patterns for a powder produced by scraping off and grinding the AACVD sulfur-deficient SnS thin film (blue = XRD pattern for SnS,^[20] green = XRD pattern for Sn^[21]); b) GIXRD pattern for the AACVD stoichiometric SnS thin film (blue = XRD pattern for SnS,^[22] pink = XRD pattern for stainless-steel substrate).

which is consistent with the literature ($a = 5.8354(8)$ Å and $c = 3.1825(5)$ Å).^[21] This powder XRD data partly explains the reason for the sulfur-deficient Sn:S ratio determined by EDX analysis. A Rietveld fit ($R_{wp} = 1.99\%$) showed 93.65% of the SnS phase (crystallite size 92 nm) and 6.35% of the Sn phase present, result shown in Figure S4, Supporting Information. With the sample composition at 93.65% of the tin sulfide phase, the calculated Sn:S atom ratio would be 53: 47. The measured EDX ratio of 63:37 would suggest that the SnS phase itself is deficient in sulfur with a composition of SnS_{0.89}, in addition to the elemental tin seen by XRD. Both fully occupied SnS and sulfur-deficient SnS_{0.89} models were subjected to Rietveld refinements (R_{wp}). The profile-weighted reliability factor did not show a significant improvement when the occupancy of sulfur was changed from SnS to SnS_{0.89}, but the sulfur atomic displacement parameter (U_{iso}) reduced from 0.047 to a much more reasonable 0.014, suggesting that the sulfur-deficient composition is a better model for the data. This is also consistent with the oxidation state (1.87) of tin determined by XANES (see later); hence, all data are consistent with the sulfur deficiency.

The morphology of the SnS rods in the sulfur-deficient phase with spheres at the ends of the rods suggested vapor–liquid–solid (VLS) growth through a reduction of precursor to molten tin and then the growth of SnS rods from material dissolved in the tin droplet. The operation of this mechanism can be verified by the EDX elemental maps shown in **Figure 4**, where tin-rich and sulfur-deficient spheres can be observed at the end of the growing SnS rod.

The GIXRD of the stoichiometric SnS thin films (Figure 3b) had lattice parameters $a = 4.289(4)$ Å, $b = 11.387(10)$ Å, and $c = 4.080(4)$ Å, also in line with the literature values mentioned above ($R_{wp} = 5.9\%$, $R_p = 4.64\%$).^[22] The b -axis, indicating the layer spacing, is notably larger than for the sulfur-deficient phase. Both sulfur-deficient and stoichiometric SnS are GeS-type, and also similar in average crystallite size as derived from XRD of 81 and 120 nm, respectively.

3.3. Electrochemistry of SnS in Sodium Half Cells

The charge–discharge behavior of the stoichiometric SnS films in sodium half-cells can be seen in Figure S5, Supporting Information. Cycling was carried out at a current density of 150 mA g⁻¹ but a capacity of just 173 mAh g⁻¹ was measured at the second reduction and 125 mAh g⁻¹ at the 50th. Electrochemical studies on this material were discontinued as the performance was not good compared with other SnS cell anodes.^[23,24] Possible reasons include lower conductivity of the stoichiometric SnS thin film and poorer electronic contact with the current collector. The nonstoichiometric sulfur-deficient SnS rods will have higher conductivity and the rod structure provides a continuous electronic pathway from the current collector to all parts of the material.

Galvanostatic cycling profiles of the sulfur-deficient SnS films in sodium half-cells (**Figure 5**) were obtained at 150 and 300 mA g⁻¹. The C rate of cell charging and discharging was calculated from the theoretical capacity of 1202 mAh g⁻¹. A very high initial capacity of 1084 mAh g⁻¹ was passed on the first

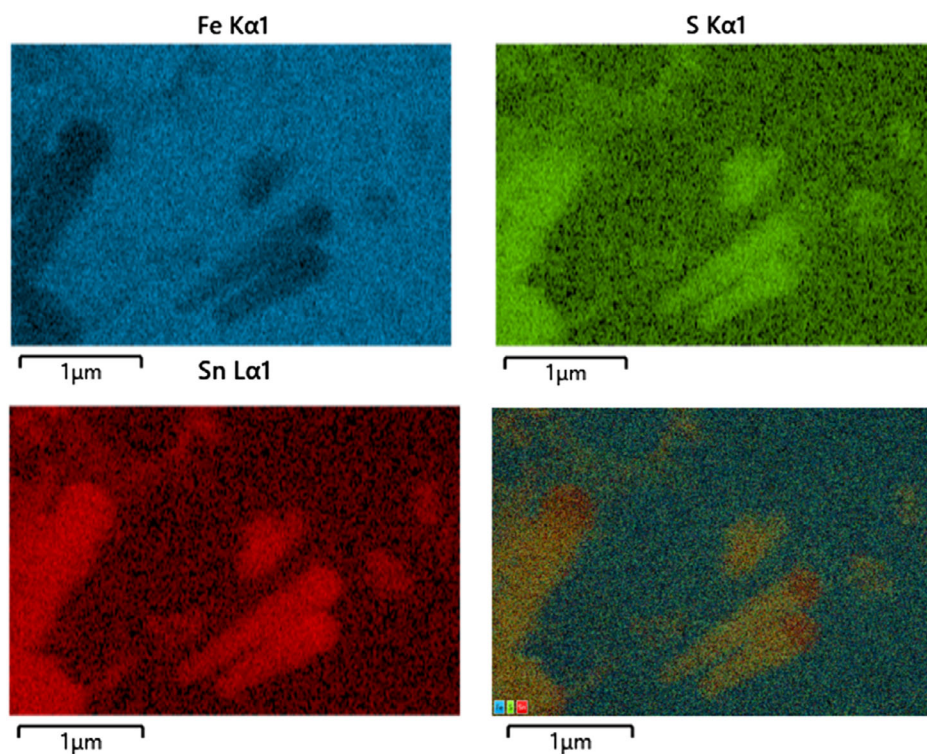


Figure 4. EDX analysis elemental mapping of Fe, tin, and sulfur across a number of growing rods, with elements labeled and the composite map (bottom right) plotted using the same colors as the individual maps.

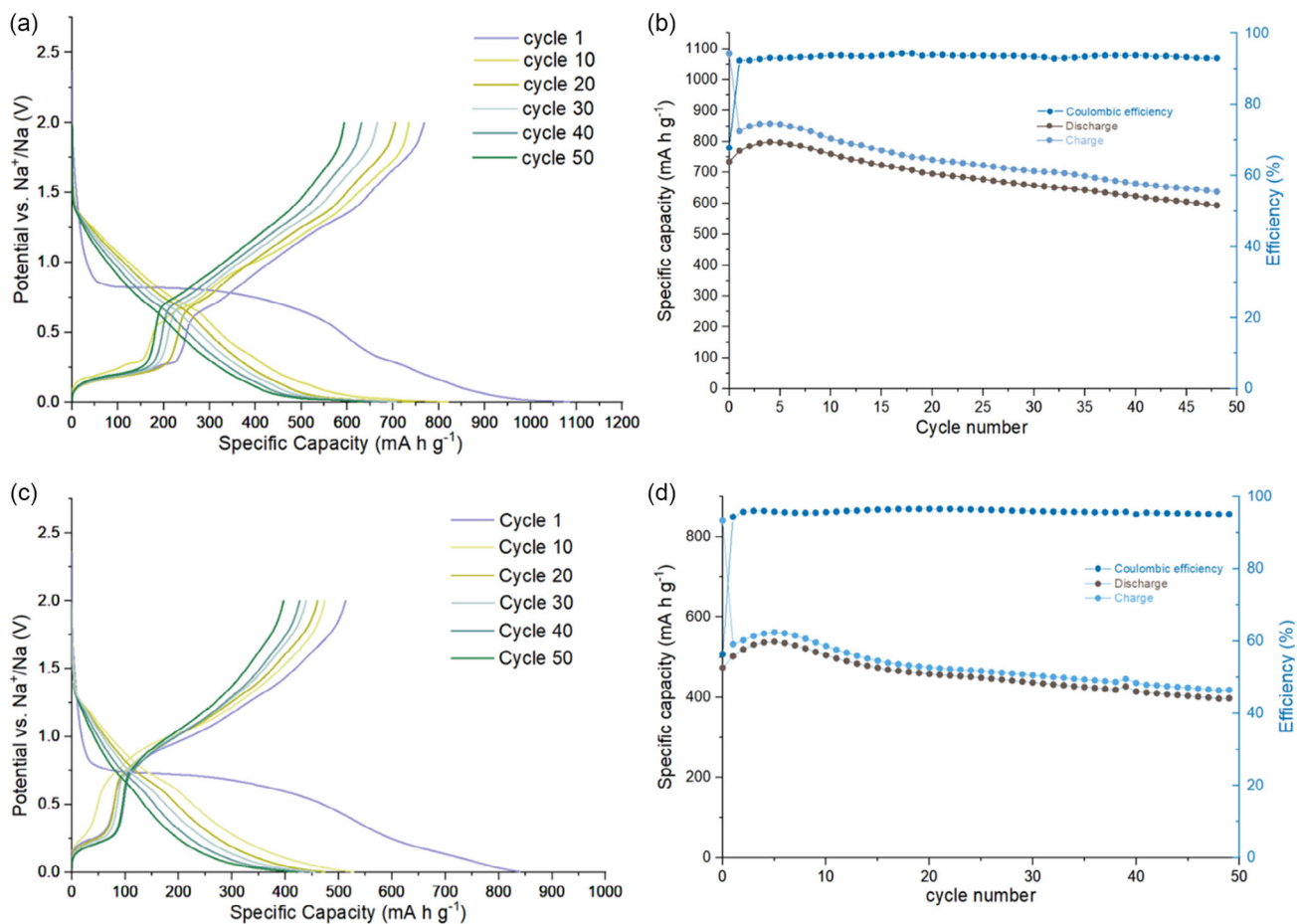


Figure 5. a,c) Potential-capacity plots during galvanostatic cycling, and b,d) plots of specific capacity and efficiency versus cycle number of sulfur-deficient SnS in Na half-cells at (a,b) 150 mA g^{-1} and (c,d) 300 mA g^{-1} .

reduction to 5 mV at a modest current of 150 mA g^{-1} ($\approx C/8$). A capacity of 735 mAh g^{-1} was recovered on the first oxidation to 2 V, close to the SnS theoretical capacity.

The low efficiency of the first reduction and oxidation was attributed to irreversible processes such as SEI formation.^[7,25] After the first cycle, subsequent cycles exhibited reversible and stable electrochemistry, with 93% charge–discharge coulombic efficiency measured after five cycles. The capacity was 638 mAh g^{-1} for reduction and 593 mAh g^{-1} for oxidation at the 50th cycle. After 50 cycles, the cell retained about 84% of the reversible oxidation capacity of the first cycle. A higher coulombic efficiency of 95% was achieved at a faster current of 300 mA g^{-1} , presumably because less reaction occurred between the electrolyte and the anode. The oxidation capacity decay between the first and 50th cycle at this higher current was 19%, from 473 to 397 mAh g^{-1} , slightly larger than the 16% loss at 150 mA g^{-1} , so reversibility of the electrode is better at low current density. A higher current of 600 mA g^{-1} was used to charge a cell over a larger number of cycles, as shown in **Figure 6a**. After 100 cycles the cell efficiency was higher than 94% and cell sodiation capacity was 368 mAh g^{-1} . The rate capabilities of sulfur-deficient SnS are displayed in **Figure 6b**. Under a lower current of 100 mA g^{-1} , a capacity of 828 mAh g^{-1} is

achieved, similar to that at 150 mA g^{-1} . With an increased charge rate of 600 mA g^{-1} , both the reduction and oxidation capacities decrease to $\approx 500 \text{ mAh g}^{-1}$ between the 15th and 20th cycle. Returning to 100 mA g^{-1} current after the 20th cycle, the cell shows a reduction capacity of 593 mAh g^{-1} and an oxidation capacity of 518 mAh g^{-1} .

The low mass loading of active material (0.1–0.4 mg) used in this study is a characteristic of the thin film material deposited using the CVD method, which is close to a single layer of crystals. Working with a low mass loading can be useful to demonstrate ultimate capacity of the material in the absence of effects due to diffusion through a porous electrode. Data for different mass loading anodes run under the same conditions can be found in **Figure S6**, Supporting Information, showing that 1.5 times SnS mass loading resulted in 1.5 times capacity.

The sulfur-deficient SnS thin film material has significantly more sodium half-cell capacity and less capacity decay than others have reported for SnS alone (**Table 1**). Higher capacity anodes than those for SnS alone have also been reported from SnS/carbon composite materials (**Table 2**) with carbon constituents such as carbon nanospheres,^[11c] carbon nanofibers^[11a,26] and graphene.^[4,27] While SnS/carbon composites exhibit capacities with contributions from both SnS and the carbon support,

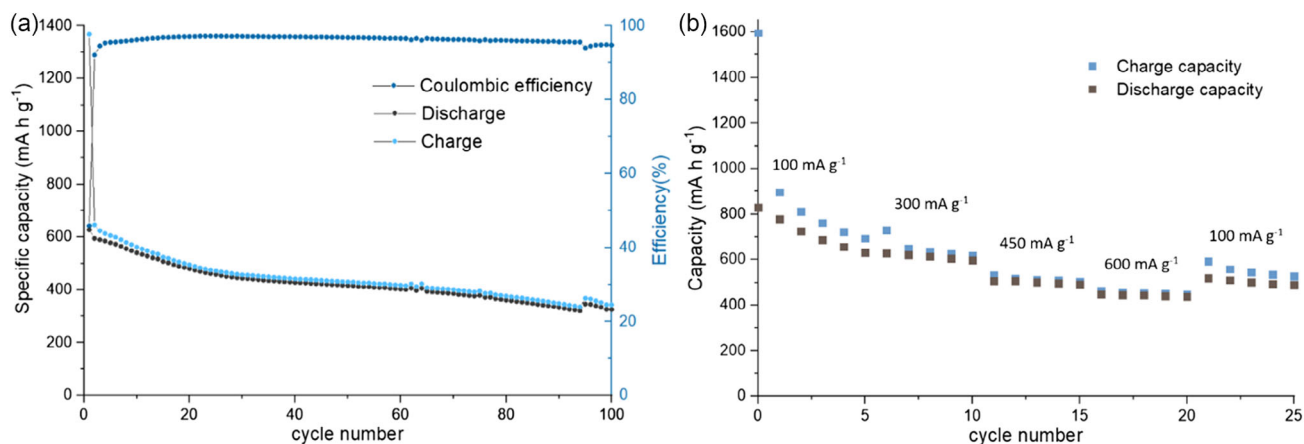


Figure 6. a) Plots of 100 cycle cell-specific capacity and efficiency versus cycle number of sulfur-deficient SnS in Na half-cells at 600 mA g⁻¹. b) Rate capabilities of sulfur-deficient SnS in Na half-cells at 100, 300, 450, and 600, then returning to 100 mA g⁻¹.

Table 2. Some high-performance examples of tin sulfide/carbon composite materials in sodium-ion anode applications.

Material	Initial discharge capacity [mAh g ⁻¹]	Final discharge capacity [mAh g ⁻¹]	Current density [mA g ⁻¹]	Number of cycles	Ref.
SnS/carbon nanospheres	280	281	100	200	[11c]
SnS/ carbon nanofibers	499.5	324	200	200	[11a]
SnS/C nanocomposite	480	445	100	50	[12]
Free-standing SnS/C nanofiber	533	481	50	100	[26]
Tubular nanocarbon/SnS nanosheets/amorphous carbon	489	411	200	80	[30]
SnS@C@rGO	366.6	312.2	5000	500	[11b]
SnS-Sn/multiwalled carbon nanotubes	1125.5	359.3	1000	1000	[31]

the capacity of sulfur-deficient SnS microrods observed here is either comparable to or surpasses these composites. This performance may be attributed, to some extent, to the higher electronic conductivity of a defective semiconductor material. However, the rod morphology is also likely to bring benefits because good electronic and ionic conduction pathways are combined with space for expansion and contraction of the rods during electrochemical cycling.

3.4. Electrochemical Reaction Mechanism of Sulfur-Deficient SnS Thin Film Anodes

The nanorod structure of the sulfur-deficient SnS presented in this study has enabled a high capacity from the sodium half-cells. Most current work focuses on developing cell performance, but fewer studies explore the material's reaction mechanism. We have probed this using ex situ XRD and XANES measurements. The samples were chosen from the derivative capacity plot (Figure S7, Supporting Information) of the first cycle with four samples prepared at various stages of reduction and five during the oxidation, as indicated in Figure 7. Before 0.75 V, there is a long plateau on the first reduction. This plateau would be expected to be due to sodium ion insertion into the SnS surface and also a conversion reaction of SnS to Sn metal.^[4] At lower potentials, we anticipate that the fully sodiated state (0.005 V vs Na/Na⁺) of the Na_xSn_y phase would be formed; this would

be matched with the alloying reaction. There is a reasonable likelihood that after the first cycle when the sample is fully oxidized (2.0 V vs Na/Na⁺), the oxidation state will be the same as that of the pristine material.

SEM and EDX analyses were used to compare the changes between the pristine material and after the first reduction and oxidation of the electrode. Compared with the starting material (Figure 2a), the crystallite morphology did not change significantly but the pristine material has longer rods than after one electrochemical cycle and the structure of the rods has become less distinct, suggesting that they may have been coated or have distorted their shapes (Figure 8a). In addition, EDX showed aluminum coming from the Al sample holder, as well as sodium from the electrolyte. The tin:sulfur atom ratio changed very little, from 62:38 (pristine) to 64:36 (post-first cycle) (Figure 8b). The 2% sulfur loss is likely to arise from the dissolution of elemental sulfur into the electrolyte as polysulfide during reduction.

In Figure 7b, the irreversible peak around 0.8 V in the first reduction can be explained as SEI layer formation. The following cycles have a reduction peak around 0.71 V and a reversible oxidation peak around 0.68 V, which can be assigned to the conversion reaction of SnS ↔ Sn. The intense peaks that are present in every cycle in reduction (0.075 to 0.005 V) and oxidation (0.01 to 0.058 V) can be attributed to sodium alloying with tin and provide a large fraction of the battery's capacity. Ex situ XRD of the

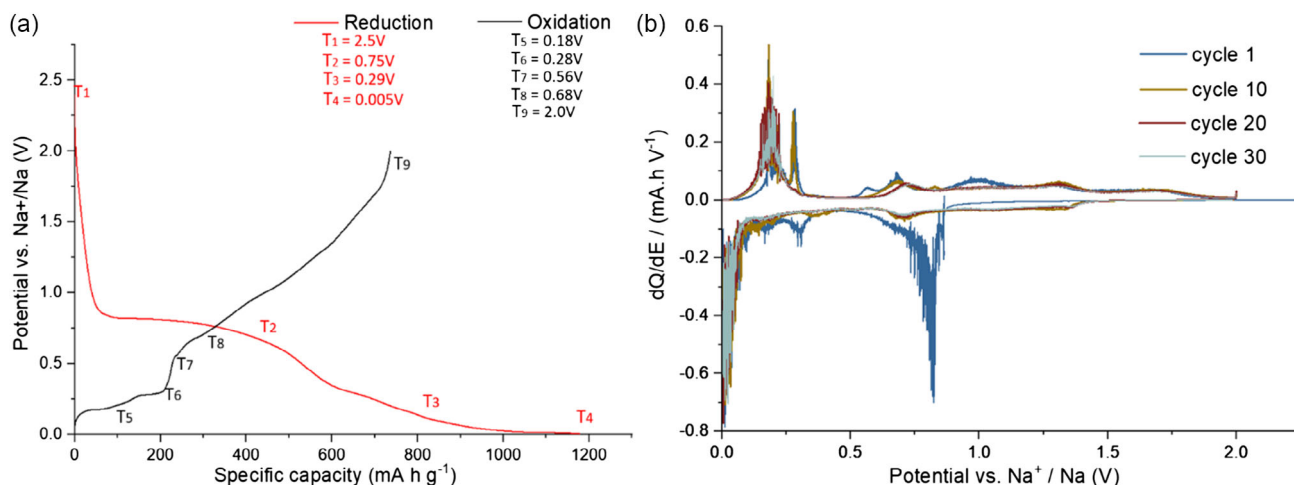


Figure 7. a) Initial galvanostatic cycle of sulfur-deficient SnS at 150 mA g^{-1} depicting where samples were taken for the ex situ XRD and XANES studies. b) dQ/dE versus potential curves obtained from sulfur-deficient SnS at the 1st, 10th, 20th, and 30th cycle.

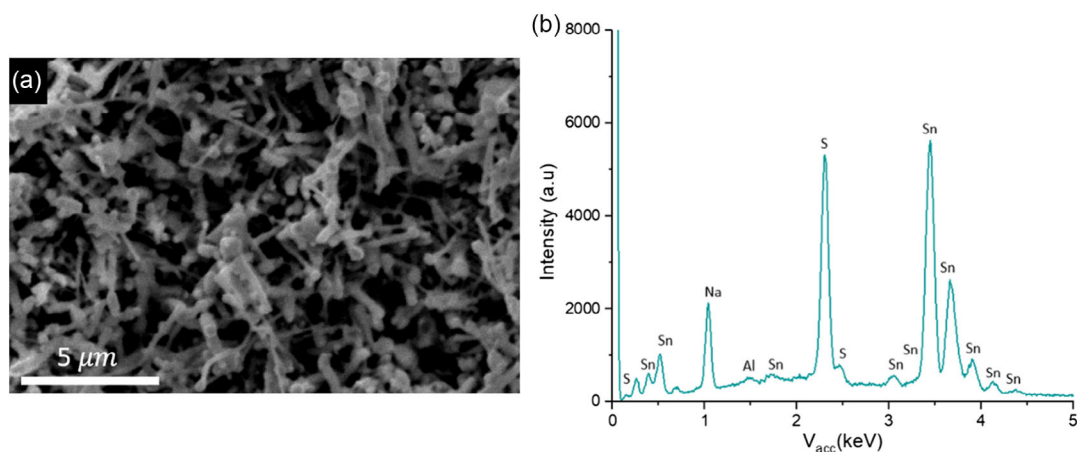


Figure 8. a) Top-view SEM image for sulfur-deficient SnS electrode after the first cycle at a specific current of 150 mA g^{-1} using $6500\times$ magnification. b) EDX spectrum obtained for a sulfur-deficient SnS electrode after the first cycle at a specific current of 150 mA g^{-1} .

products of the first reduction and oxidation reactions are shown in **Figure 9**. Uncharged electrodes show clear reflections due to SnS and all of these peaks (especially $2\theta = 31.5^\circ$) gradually diminish in intensity in the process of initial sodiation. Meanwhile, metallic Sn peaks ($2\theta = 31.9^\circ$) were observed in an electrode reduced to 0.75 V versus Na/Na⁺, as predicted by the conversion process. The intensity of the tin metal peaks increased through the plateau at 0.8 V versus Na/Na⁺ in **Figure 7**. Upon further reduction to 0.005 V versus Na/Na⁺, SnS peaks continually decreased ($2\theta = 31.5^\circ$) and the Sn peaks increased ($2\theta = 31.9^\circ$) in intensity. The characteristic Na₂S peak at $2\theta = 36.3^\circ$ in **Figure 9** occurs alongside two plateaus at 0.4 and 0.1 V versus Na/Na⁺ in **Figure 7**, which means this is associated with the alloying reaction where tin metal was intercalated with sodium ions to form sodium tin alloy. However, using XRD it is difficult to define which Na–Sn alloy phases were produced due to the thickness of the thin film and the very small amount of crystalline material formed. This will be further explored in the XANES discussion below.

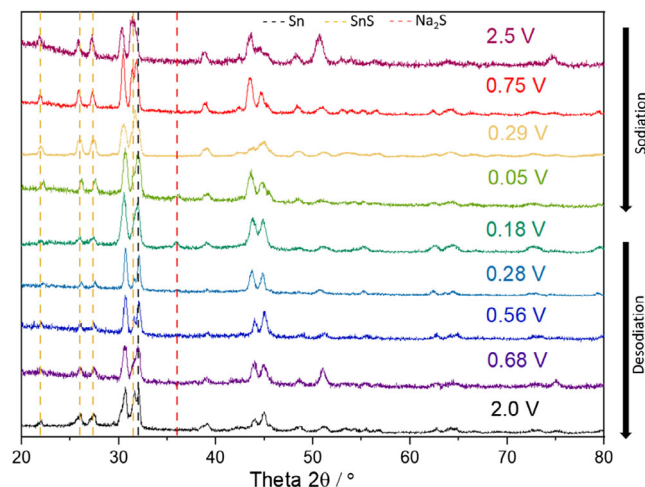


Figure 9. Ex situ XRD patterns of sulfur-deficient SnS during the first sodiation and desodiation process, with samples produced at the potentials shown and as described in **Figure 7**.

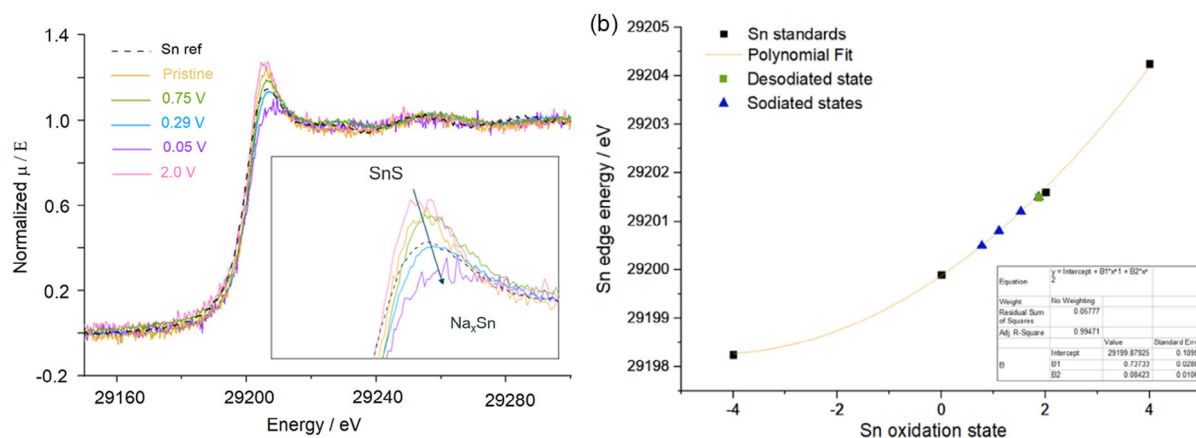


Figure 10. a) Sn K-edge XANES spectra during first sodiation/desodiation (insets: white line of the absorption edge); b) oxidation state fitted with Sn K-edge energies.

On desodiation, the SnS signal in the XRD (Figure 9) became stronger (especially $2\theta = 31.5^\circ$), and was the same height as the Sn peak after the sample was fully oxidized (2.0 V vs Na/Na⁺). This change implies that SnS reduction and oxidation are reversible. The reversible SnS peaks and the high Sn peak correspond to the 2% increase in Sn observed in the EDX analysis above, showing a reverse to SnS. This result is consistent with other orthorhombic-SnS anodes, but in this case, SnS peaks change more significantly.^[12] Other researchers report the disappearance of Sn during the desodiation, but not the reversible observation of SnS.^[4,11c]

Operando XANES on the Sn K-edge, **Figure 10a**, shows a continuous decrease in white line peak height (based on data normalized to the EXAFS region) from the uncharged pristine sample (highest in white line) to the height of the tin reference and then lower still during sodiation. Yu et al. noted the white line intensity continually drops with a reducing tin oxidation state.^[12] Compared with a tin standard, the sample collected during reduction at 0.29 V versus Na/Na⁺ had a lower intensity white line, indicating the completion of the conversion reaction from SnS to Sn (Equation (1)). It should be recognized that XANES is an averaging technique so this shows the average oxidation state if the sample has any inhomogeneity. At the fully reduced state (0.005 V vs Na/Na⁺), the white line intensity further decreased; this would be explained as further sodiation processes (alloying). Figure 10a also shows the highest white line position of the sample at a fully oxidized state (2.0 V vs Na/Na⁺), which means the sample after the oxidation was fully reversible to a higher oxidation state. The oxidation state was also compared, based on Sn K-edge energy, with Sn (0), SnS (+2), SnO₂ (+4), SnO (+2), Sn (0), and Na₄Sn (−4) standards. The sulfur-deficient SnS material decreased from an average oxidation state of +1.87 to 0.78 (Table S2, Supporting Information), then back to the same oxidation state as the uncharged sample.

From the XANES, there was a reduction in the oxidation state on sodiation but this returned to its original value when the cell finished the first cycle at 150 mA g^{−1}. This is consistent with the EDX and exsitu XRD data, which show that sodium sulfide can be converted back to tin sulfide in the oxidation reaction. Although neither the XRD nor XANES show which

sodium–tin alloy phase the SnS material is converted to during reduction, between them they prove that SnS conversion and alloying are reversible. The loss of a small quantity of sulfur suggests Sn was produced during the desodiation process, and the large capacity of the sodium half-cells was at least partially due to the extra tin present in this material. The increase in capacity over the first five cycles (Figure 5) suggests that an increase in the non-stoichiometry of the tin sulfide phase was beneficial to capacity.

4. Conclusion

Sulfur-deficient SnS films were obtained through AACVD directly onto stainless steel foil with good substrate coverage. Samples consisted of ≈100 nm diameter rods of SnS_{0.89} with some tin contamination due to VLS growth. Electrodes were cut from this foil for assessment in sodium half-cells. The sulfur-deficient rod structure provides a higher capacity and better cycling stability than other SnS-only materials. This improved performance can be attributed directly to the SnS film itself, while the other high capacity SnS materials reported previously are all composites with carbon supports.

The mechanism was investigated by ex situ XRD and XANES analyses showing a reversible oxidation and reduction reaction of this sulfur-deficient SnS thin film material. The contributions of this study include a new tin sulfide anode synthesis method via AACVD from single source precursors, a new kind of tin sulfide anode, and a study of the operating mechanism of this material, and offer good prospects for further SIBs development.

Supporting Information

Supporting Information is available from the Wiley Online Library or from the author.

Acknowledgements

The authors thank Diamond Light Source for the award of beam time as part of the Energy Materials Block Allocation Group SP14239, and EPSRC for funding under EP/K00509X/1, EP/K009877/1, and EP/V007629/1.

Conflict of Interest

The authors declare no conflict of interest.

Author Contributions

Z.Z.: Investigation, data producer, writing—original draft. A.L.H.: Supervision, project administration, writing—review and editing. G.H.: AACVD part supervision, writing—review and editing. G.R.: Precursor part supervision, writing—review and editing. F.R.: Precursor part cooperater, writing—review. G.C.: XANES data collector, writing—review and editing.

Data Availability Statement

The data that support the findings of this study are openly available in University of Southampton data repository at <https://doi.org/10.5258/SOTON/D2541>.

Keywords

aerosol-assisted chemical vapor deposition (AACVD), sodium-ion batteries, tin sulfide, X-ray absorption near-edge structure (XANES)

Received: December 18, 2022

Revised: February 12, 2023

Published online:

- [1] a) S. Roberts, E. Kendrick, *Nanotechnol. Sci. Appl.* **2018**, *11*, 23; b) H. Zhang, I. Hasa, S. Passerini, *Adv. Energy Mater.* **2018**, *8*, 1702582.
- [2] a) V. Palomares, P. Serras, I. Villaluenga, K. B. Hueso, J. Carretero-González, T. Rojo, *Energy Environ. Sci.* **2012**, *5*, 5884; b) M. D. Slater, D. Kim, E. Lee, C. S. Johnson, *Adv. Funct. Mater.* **2013**, *23*, 3255; c) S. W. Kim, D. H. Seo, X. Ma, G. Ceder, K. Kang, *Adv. Energy Mater.* **2012**, *2*, 710.
- [3] Z. Zhang, X. Zhao, J. Li, *Electrochim. Acta* **2015**, *176*, 1296.
- [4] T. Zhou, W. K. Pang, C. Zhang, J. Yang, Z. Chen, H. K. Liu, Z. Guo, *ACS Nano* **2014**, *8*, 8323.
- [5] a) H. Hou, X. Qiu, W. Wei, Y. Zhang, X. Ji, *Adv. Energy Mater.* **2017**, *7*, 1602898; b) J. Wang, Y.-S. Li, P. Liu, F. Wang, Q.-R. Yao, Y.-J. Zou, H.-Y. Zhou, M.-S. Balogun, J.-Q. Deng, *J. Cent. South Univ.* **2021**, *28*, 361.
- [6] a) A. Darwiche, C. Marino, M. T. Sougrati, B. Fraisse, L. Stievano, L. Monconduit, *J. Am. Chem. Soc.* **2012**, *134*, 20805; b) M. Lao, Y. Zhang, W. Luo, Q. Yan, W. Sun, S. X. Dou, *Adv. Mater.* **2017**, *29*, 1700622; c) Z. Li, J. Ding, D. Mitlin, *Acc. Chem. Res.* **2015**, *48*, 1657; d) H. Mou, W. Xiao, C. Miao, R. Li, L. Yu, *Front. Chem.* **2020**, *8*, 141.
- [7] S. D. Fitch, G. Cibir, S. P. Hepplestone, N. Garcia-Araez, A. L. Hector, *J. Mater. Chem. A* **2020**, *8*, 16437.
- [8] a) L. Wu, Z. Xie, L. Lu, J. Zhao, Y. Wang, X. Jiang, Y. Ge, F. Zhang, S. Lu, Z. Guo, *Adv. Opt. Mater.* **2018**, *6*, 1700985; b) S. Hegde, A. Kunjomana, P. Murahari, B. Prasad, K. Ramesh, *Surf. Interfaces* **2018**, *10*, 78; c) S. Bashkurov, V. Gremenok, V. Ivanov, V. Lazenka, K. Bente, *Thin Solid Films* **2012**, *520*, 5807.
- [9] Y. Shan, Y. Li, H. Pang, *Adv. Funct. Mater.* **2020**, *30*, 2001298.
- [10] Y. Xiao, S. H. Lee, Y. K. Sun, *Adv. Mater.* **2017**, *7*, 1601329.
- [11] a) H. Yan, M. Yang, L. Liu, J. Xia, Y. Yuan, J. Liu, Y. Zhang, S. Nie, X. Wang, *J. Alloys Compd.* **2020**, *843*, 155899; b) L.-B. Tang, P.-Y. Li, T. Peng, H.-X. Wei, Z. Wang, H.-Y. Wang, C. Yan, J. Mao, K. Dai, X.-W. Wu, *J. Electroanal. Chem.* **2023**, *928*, 117077; c) G. K. Veerasubramani, M.-S. Park, J.-Y. Choi, D.-W. Kim, *ACS Appl. Mater. Interfaces* **2020**, *12*, 7114.
- [12] S.-H. Yu, A. Jin, X. Huang, Y. Yang, R. Huang, J. D. Brock, Y.-E. Sung, H. D. Abruña, *RSC Adv.* **2018**, *8*, 23847.
- [13] a) L. S. Price, I. P. Parkin, A. M. Hardy, R. J. Clark, T. G. Hibbert, K. C. Molloy, *Chem. Mater.* **1999**, *11*, 1792; b) C. De Groot, C. Gurnani, A. L. Hector, R. Huang, M. Jura, W. Levason, G. Reid, *Chem. Mater.* **2012**, *24*, 4442.
- [14] F. Robinson, P. J. Curran, C. K. de Groot, D. Hardie, A. L. Hector, K. Holloway, R. Huang, D. Newbrook, G. Reid, *Mater. Adv.* **2021**, *2*, 4814.
- [15] M. R. Waugh, G. Hyett, I. P. Parkin, *Chem. Vap. Dep.* **2008**, *14*, 366.
- [16] a) I. Parkin, L. Price, T. Hibbert, K. Molloy, *J. Mater. Chem.* **2001**, *11*, 1486; b) B. P. Bade, S. S. Garje, Y. S. Niwate, M. Afzaal, P. O'Brien, *Chem. Vap. Dep.* **2008**, *14*, 292.
- [17] I. Database, in ICS Database, Vol. FIZ, Karlsruhe Germany, **2008**.
- [18] B. H. Toby, R. B. Von Dreele, *J. Appl. Crystallogr.* **2013**, *46*, 544.
- [19] F. Davitt, K. Stokes, T. W. Collins, M. Roldan-Gutierrez, F. Robinson, H. Geaney, S. Biswas, S. L. Chang, K. M. Ryan, G. Reid, *ACS Appl. Energy Mater.* **2020**, *3*, 6602.
- [20] W. Hofmann, *Z. Kristallogr. Cryst. Mater.* **1935**, *92*, 161.
- [21] V. Deshpande, D. Sirdeshmukh, *Acta Crystallogr.* **1962**, *15*, 294.
- [22] T. Chattopadhyay, J. Pannetier, H. Von Schnering, *J. Phys. Chem. Solids* **1986**, *47*, 879.
- [23] P. K. Dutta, U. K. Sen, S. Mitra, *RSC Adv.* **2014**, *4*, 43155.
- [24] E. Cho, K. Song, M. H. Park, K. W. Nam, Y. M. Kang, *Small* **2016**, *12*, 2510.
- [25] a) R. Mogensen, D. Brandell, R. Younesi, *ACS Energy Lett.* **2016**, *1*, 1173; b) E. M. Lotfabad, P. Kalisvaart, A. Kohandehghan, D. Karpuzov, D. Mitlin, *J. Mater. Chem. A* **2014**, *2*, 19685.
- [26] J. Xia, L. Liu, S. Jamil, J. Xie, H. Yan, Y. Yuan, Y. Zhang, S. Nie, J. Pan, X. Wang, *Energy Storage Mater.* **2019**, *17*, 1.
- [27] J. Shi, Y. Wang, Q. Su, F. Cheng, X. Kong, J. Lin, T. Zhu, S. Liang, A. Pan, *Chem. Eng. J.* **2018**, *353*, 606.
- [28] M. Dogrusoz, R. Demir-Cakan, *Int. J. Energy Res.* **2020**, *44*, 10809.
- [29] H. Jia, M. Dirican, N. Sun, C. Chen, P. Zhu, C. Yan, X. Dong, Z. Du, J. Guo, Y. Karaduman, *Chem. Commun.* **2019**, *55*, 505.
- [30] H. Ding, Y. Wu, Y. Xia, T. Yang, Z. Hu, Q. Chen, G. Yue, *J. Mater. Sci.* **2022**, *57*, 6308.
- [31] Y. Sun, Y. Yang, X.-L. Shi, G. Suo, H. Chen, X. Hou, S. Lu, Z.-G. Chen, *ACS Appl. Mater. Interfaces* **2021**, *13*, 28359.